

# COMPUTATIONAL MODELING AND EXPERIMENTAL VALIDATION OF MELTING AND SOLIDIFICATION IN EQUIAXED SUPERALLOYS PROCESSED THROUGH SCANNING LASER EPITAXY

Amrita Basak\*, Ranadip Acharya\*, Rohan Bansal\*, and Suman Das\*

\* George W. Woodruff School of Mechanical Engineering, Georgia Institute of Technology, Atlanta, GA 30332

## Abstract

This paper focuses on simulation-based optimization of the Scanning Laser Epitaxy (SLE) process applied to gas turbine hot-section components made of nickel-base superalloys. SLE creates equiaxed, directionally-solidified and single-crystal microstructures from superalloy powders melted onto like-chemistry substrates using a fast scanning, high power laser beam. In this paper, a transient coupled flow-thermal approach is implemented to accurately simulate the melting and solidification process in SLE. The laser movement is modeled as a Gaussian moving heat source, and the thermophysical properties of the alloys are adjusted based on the thermal field. Simulations for different superalloys such as IN100, René 80 and MAR-M247 are performed and the instantaneous melt pool characteristics are recorded. Comparisons of the simulations with experimental results show reasonably good agreement for the melt depth. Feedback control is implemented, and demonstrated to produce superior quality SLE deposits. This work is sponsored by the ONR through grants N00014-11-1-0670 and N00014-14-1-0658.

## Introduction

The design life of commercial gas-turbine engine hot-section components is typically shorter than their cold section counterparts, primarily because of their significantly elevated operating temperatures. The ever increasing demand for operating modern state-of-the-art engines at higher temperatures has put forward a challenging task for engineers to design suitable materials for these components. Material issues are of paramount significance for these components. Currently nickel-base superalloys are used to manufacture these parts as they offer higher yield strength with increasing operating temperatures primarily due to the presence of the secondary  $\gamma'$  phases that form an antiphase boundary and lock the associated dislocation movements. The degradation of the hot-section components are attributed to creep, thermo-mechanical fatigue, high temperature oxidation, and thermal corrosion. Currently, the lack of suitable commercial repair technologies results in high maintenance costs for these components that can reach as much as hundreds of thousands to even millions of dollars per engine. Hence, there is a great commercial interest in additive manufacturing processes capable of restoring the parent metallurgical microstructure and geometry at damage locations for these parts. This paper focuses on simulation-based process development for scanning laser epitaxy (SLE); a laser based additive manufacturing process that has demonstrated the capability of repairing these high-value parts.

SLE is a metal powder bed fusion-based additive manufacturing process that creates equiaxed (EQ), directionally solidified (DS) and single-crystal (SX) structures in nickel superalloys through controlled laser melting of alloy powders onto like chemistry substrates. In

SLE, a galvanometer controlled high power laser beam is directed onto the powder bed. Processing parameters such as laser power, preheat and scan speed are varied in SLE to control and optimize the deposit characteristics. An important criterion for a successful SLE deposit is the determination of energy density that ensures a good metallurgical bond between the substrate and the deposit along the entire length of the substrate. The metallurgical bond starts at one edge of the substrate where the melt pool is initiated. The melt pool travels across the length of the substrate fusing the powder to the substrate. Under the proper operating conditions, the solidified microstructure has been demonstrated to nucleate from and follow the morphology of the underlying substrate.

Computational modeling and simulation of the SLE process can provide critical insights into the physics of the process and help in determining the desired operating parameters for different superalloy powders, thereby reducing the number of experimental runs. Several reports on the simulation of laser-based additive manufacturing approaches can be found in literature. Both Finite Element Methods (FEM) and Finite Volume Methods (FVM) are used for the thermal modeling of the system [1, 2]. Gäumann implemented a modified Rosenthal solution [3] and obtained the liquid isotherm and a circular melt pool [4]. Christensen et al. has suggested the formation of an elliptic melt pool along the direction of the beam's movement [5]. Goldak et al. assumed a double-ellipsoid weld pool shape that consists of front and rear ellipsoid quadrants [6]. A coupled thermal-flow model allows incorporation of fluid convection inside the melt pool. To model the flow pattern prevailing inside the melt pool, surface tension driven flow known as Marangoni convection (or Bernard-Marangoni convection) is typically included in the flow-thermal model [7]. Inclusion of Marangoni convection extends the melt pool laterally and makes it shallower [8, 9]. Acharya et al. [10] developed a three-dimensional CFD model and obtained good agreement with experimental data for the melt depth in single-crystal alloy CMSX-4 processed through SLE. Acharya et al. implemented a pseudo-2D approach to model the melt pool characteristics for IN100 and obtained reasonably good agreement for the melt depth and the average melt pool temperature [11].

In this work, Acharya's pseudo-2D CFD model [11] has been extended to simulate and compare the melt pool characteristics for different equiaxed superalloys. The movement of the laser beam along the x and y directions is modeled as a line source scanning in the x direction. The laser power profile in the y-direction is modeled from the transient averaged data for a single scan and approximated with a 10th degree polynomial [11]. This polynomial is found to be flat in the middle region with some reduction of intensity near the edges of the sample. This characteristic of the power profile justifies the simplification of the computationally expensive three-dimensional CFD model to a tractable two-dimensional simulation. The width of the coupon is used to calculate the residence time of the line heat source at any given position, and then the heat source is advanced in the forward direction by the scan spacing. The complete scan pattern is formulated using ANSYS CFX user-defined functions. The heat conduction equation is used to model the transfer of heat to the base plate. Analysis of the flow-field modeling reveals the formation of rotational vortices due to the moving heat source and the Boussinesq convection. Reasonable agreement between the simulation and the experimental results is achieved for the melt depth for different superalloy powders. The effect of SLE operating parameters on the melt depth has been analyzed and presented in this work.

## SLE Experimental Procedure

SLE processing of the nickel-base superalloys such as IN100, René 80 and MARM-247 is investigated in this work. The René 80 and MARM-247 powders are produced by Praxair Surface Technologies using an atomization process. The IN100 powder is produced by HMI Metal Powders using Argon gas atomization. Table 1 summarizes the chemical composition of these superalloy powders.

**Table 1.** Chemical composition of various superalloys (wt. %)

	Cr	Co	Mo	Re	W	Al	Ti	Ta	Hf	B	C	Zr	Ni
IN100	10.0	15.0	3.0	-	-	4.7	5.5	-	-	0.014	0.18	0.06	Bal
René 80	14.0	10.0	4.0	-	4.0	3.0	5.0	-	-	-	-	-	Bal
MARM-247	8.0	10.0	-	-	10.0	6.0	1.0	3.0	1.0	-	-	-	Bal

The SLE process is conducted on EQ cast rectangular coupons. Coupon dimensions for IN100 and René 80 are 35.56mm X 6.86mm X 2.54mm while for MAR-M247 the coupons are slightly smaller in size having dimensions of 31.50mm X 5.84mm X 2.54 mm. Each substrate is placed into a 35.56mm x 6.86mm (for IN100 and René 80) and 31.50mm X 5.84mm (for MAR-M247) recess cut into an Inconel 625 base plate. A powder bed is placed atop the substrate using rectangular wells cut into an Aluminum mask plate. Once the samples are prepared, they are placed into an atmospheric process chamber that is purged with high purity (99.999%) Argon. A 1kW Ytterbium fiber laser (IPG Photonics, Model: YLS-1000) is used along with a Cambridge Technologies galvanometer scanner to scan the beam on the powder bed. The beam is focused to a 40  $\mu\text{m}$  Gaussian diameter. A raster scan pattern across the width of the sample generates a melt pool that linearly propagates along the length of the substrate. The details of the experimental setup can be found elsewhere [11], and is skipped here for brevity.

## SLE Deposit Characterization

SLE-processed samples are sectioned along the length and width for metallography. A Buehler automated saw is used to cut the samples. A Leica DM6000 optical microscope is thereafter used to take the images. Figure 1 (a) and 1 (b) demonstrate lengthwise cross-sectional view of crack-free IN100 and René 80 samples as processed by SLE showing a full metallurgical bond along the entire length of the sample.

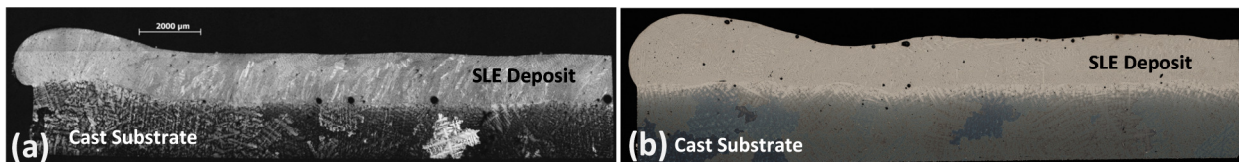


**Figure 1.** Representative lengthwise section of the first half of a (a) IN100 and (b) René 80 samples with the starting edge on the left side of the image.

## Computational Flow-Thermal Modeling of SLE

A transient, multi-domain model with temperature-dependent property values is used to simulate the flow-thermal behavior of the SLE and to predict the melt pool characteristics. Temperature-dependent thermo-physical property data for IN100, René 80 and MAR-M247 is modeled using tabular data [11, 12]. The pseudo-2D model includes two separate domains – (1) the deposit domain consisting of the substrate and the powder and (2) the Inconel baseplate domain. Figure 2 shows the geometry and the mesh for the 2D configuration. The deposit domain has a finer mesh to accurately capture the 20 micron radius laser heat source. The total node count of the mesh is close to 137k and the skewness is below 0.2. The simulation is performed in ANSYS CFX solver.

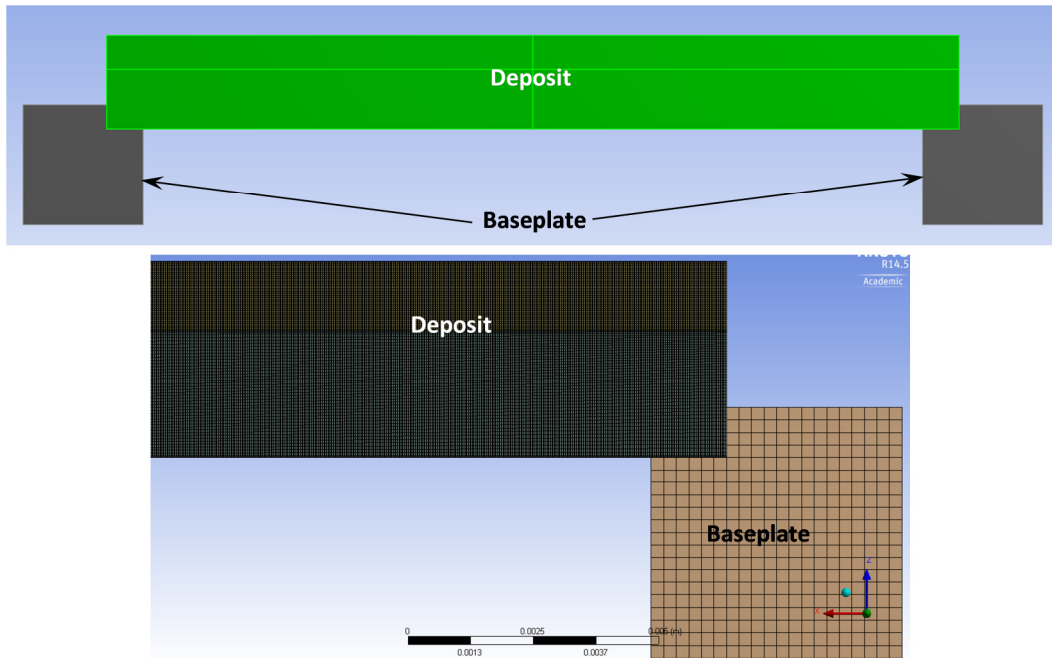


**Figure 2.** ANSYS CFX simulation model showing different domains – Deposit domain and Baseplate domain.

The solid and liquid component enthalpy equations, expressed in terms of volume fraction,  $r$ , are:

$$\frac{\partial(\rho_S r_S h_S)}{\partial t} + \nabla \cdot (\rho_S r_S \underline{U}_S h_S) = \nabla \cdot (r_S k_S \nabla T_S) + I \quad (1a)$$

$$\frac{\partial(\rho_L r_L h_L)}{\partial t} + \nabla \cdot (\rho_L r_L \underline{U}_L h_L) = \nabla \cdot (r_L k_L \nabla T_L) - I \quad (1b)$$

Here  $\rho$  is the density,  $h$  is the enthalpy (including the latent heat),  $T$  is the temperature,  $U$  is the velocity and  $I$  is the interphase heat transfer. The subscripts S and L refer to the solid and

liquid components respectively. Equations (1a) and (1b) can also be expressed more compactly as:

$$\frac{\partial(\bar{\rho}h)}{\partial t} + \nabla \cdot (\bar{\rho}\underline{U}h) = \nabla \cdot (\bar{k}\nabla T) - \nabla \cdot (\bar{\rho}Y_s(\underline{U} - \underline{U}_s)(h_L - h_s)) + S \quad (2)$$

Here  $\bar{\rho}$  is mixture density,  $h$  is the mixture enthalpy,  $\bar{k}$  is mixture conductivity,  $Y_s$  is the mass fraction of solid [13]. The final term of Equation (2) represents an additional source due to the difference in velocity between the solid and liquid components. This term has a finite value in the mushy region of the flow ( $0 < Y_s, Y_L < 1$ ). In the regions of pure liquid or pure solid, the mixture enthalpy equation reduces to the appropriate component enthalpy equation. The volume fractions of liquid and solid component are incorporated using tabular data representing solid and liquid fraction of the superalloys in the melting range. The Boussinesq approximation is implemented to model the effect of variable liquid density.

A Darcy like source term is incorporated to model the resistance to flow in the mushy region. The permeability is modelled using Kozeny-Carman equation [14]. To prevent division by zero, the term is bounded by a user-specified maximum,  $C$ .

$$\underline{S}_M = \min\left(C, \frac{\mu_L (1 - r_L)^2}{K_0 r_L^3}\right)(\underline{U} - \underline{U}_s) \quad (3)$$

In the turbulence equations, sink terms similar to the Darcy term in the momentum equation are applied to damp the turbulence in solid regions [13].

$$S_k = -\frac{\mu_L (1 - f_L)^2}{K_0 f_L^3} k, \quad S_\epsilon = -\frac{\mu_L (1 - f_L)^2}{K_0 f_L^3} \epsilon \quad (4)$$

For the baseplate domain, the conduction heat equation is solved.

$$\frac{\partial(\rho H)}{\partial t} = \nabla \cdot (K \nabla T) + S_0 \quad (5)$$

Here  $\rho$  is the density,  $H$  is the enthalpy,  $K$  is the thermal conductivity and  $S_0$  is the source/sink term.

The conservation of thermal energy is achieved at all interfaces. The convection heat loss is modeled as a surface sink term using Newton's law of cooling. Radiation loss is modeled using a sink term. The transient model is solved using a time-step value approximately equal to 0.002 s. The inclusion of convection, phase change model and Darcy sink term requires a smaller time-step value for solver stability. The convergence is assured once the RMS value of residual is reduced below  $10e-4$ . Once solved, the result is post-processed in CFD-post to analyze the melt pool nature, the melt depth profile and the temperature distribution.

## Results and Discussion

Computational simulation of the SLE process sheds light on the flow-thermal field generated by the moving heat source as it traverses across the substrate. The flow field affects the melt pool formation and the temperature distribution within the melt pool. Figures 3(a) and 3(b) show the velocity and temperature distribution inside the melt pool for IN100 respectively. The melt pool is identified in the regions with liquid IN100 mass fraction of 0.99 or more. This calculation is validated by the fact that inside the melt pool, the temperature is greater than 1639K, the liquidus temperature of IN100.

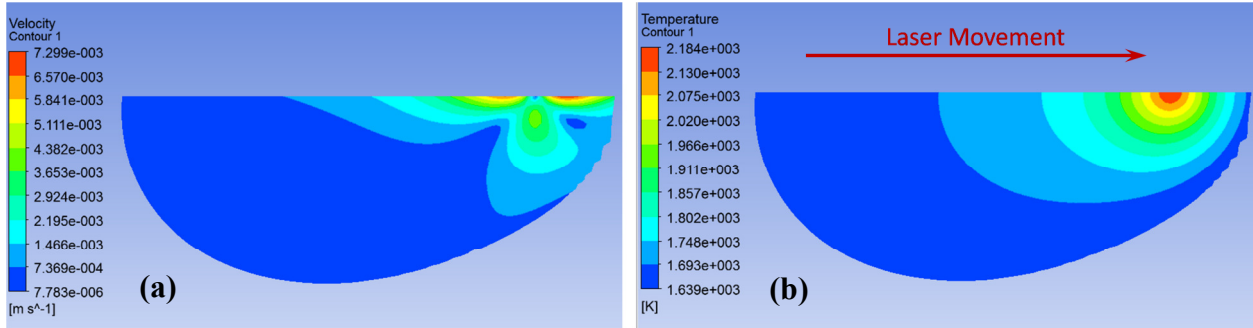


**Figure 3.** (a) Contour of velocity, (b) Contour of temperature inside the melt pool for IN100.

Figures 4(a) and 4(b) show the zoomed view of the temperature contour near the laser source with and without velocity streamlines superimposed. The melt pool consists of two counter rotating vortices with their center located approximately at the location of the laser heat source. The flow field draws loose powder at the top and feeds the melt pool as it expands.

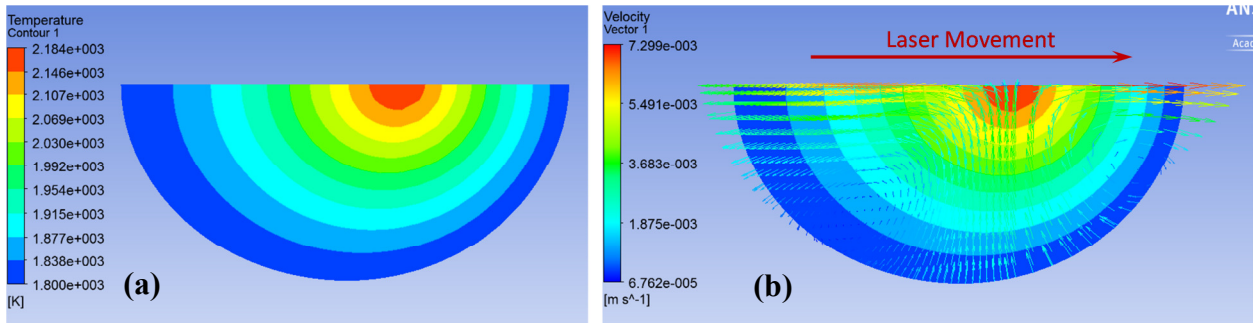


**Figure 4.** (a) Contour of temperature, (b) Velocity vector overlaid on the contour of temperature inside the melt pool for IN100.

### Characterization of SLE Melt Pool Depth

The melt depth profile is of particular interest for the present application and hence compared with the actual cross-sectional optical micrographs. Figure 5 demonstrates the melt depth comparison between simulation and experimental results for IN100, René 80 and MAR-

M24. Good agreement is obtained between simulation and experiment results for different superalloys.

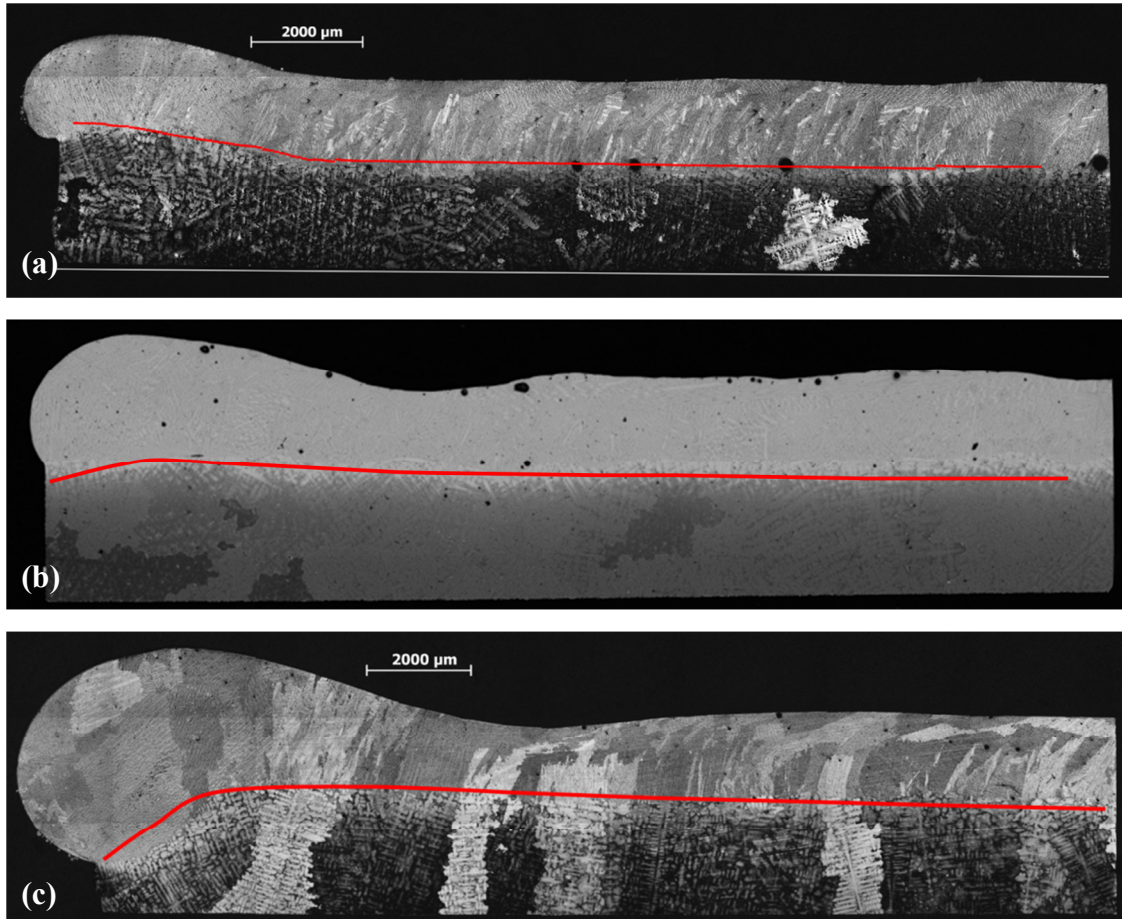


**Figure 5.** Comparison of the simulated melt depth (red line) with actual micrograph for (a) IN100 (b) René 80, and (d) MAR-M247.

### **Effect of Processing Parameters on SLE Deposit**

Characterizing the effect of SLE processing parameters on the melt pool depth is critical for understanding and control of the process. Several CFD simulations are performed with varying SLE processing parameters and the melt depth profile is obtained for IN100. The parameter range that is explored in this study includes repeat scans of 75-125, scan speeds of 300-500 mm/sec, laser powers of 300-500 W. All samples are run with a scan spacing of 25.4  $\mu\text{m}$  to account for the smaller beam diameter of the fiber laser. The effect of these parameters on the CFD-simulated average melt depth is analyzed and presented in Fig. 6. The blue dotted lines represent the 95% confidence intervals for the experimental data [11], black circles represent the CFD simulated data points, and the black line denotes the best-fit line generated from the CFD simulated data points. The nominal SLE run is performed with number of repeat scans of 100, scan speed of 400 mm/s and laser power of 400 W. The experimental and the CFD data points for the melt pool depth are normalized by the corresponding nominal SLE run. The prediction shows excellent agreement with the experimental data across the entire range of the experimental

data points. It can be seen from Fig. 6 (b) that laser power impacts the melt pool depth significantly. With increasing laser power, the melt pool extends laterally and transversely, thereby increasing the melt depth. Increasing the scan speed adversely affects the melt depth [Fig. 6 (a)]. This is primarily due to the fact that with increasing the scan speed, the laser heat source spends less time per unit surface area in processing the substrate and powder; and therefore the melt depth decreases. Increasing the number of repeat scans increases the melt pool depth at the leading edge of the substrate, and therefore increases the average melt depth [Fig. 6 (c)].

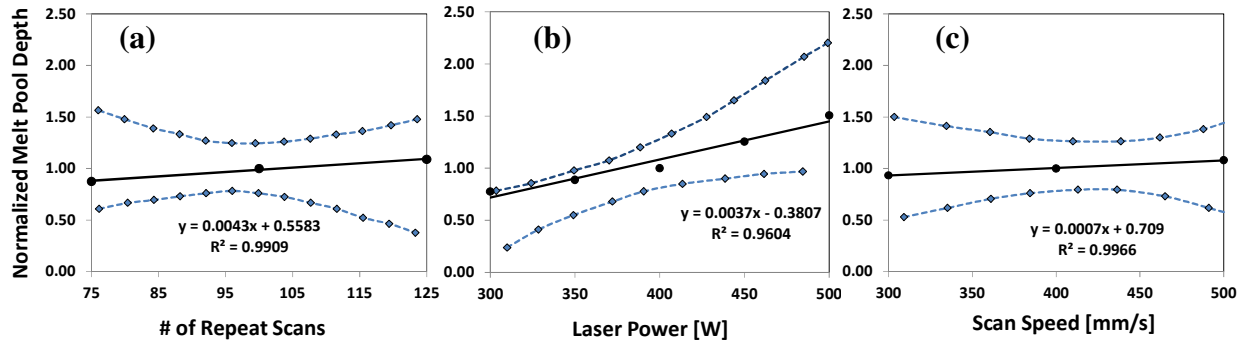


**Figure 6.** Effect of process parameters on SLE deposit characteristics – (a) Effect of scan speed, (b) Effect of laser power and (c) Effect of number of repeat scans for IN100.

### Effect of Feedback Control on SLE Deposit

The laser heat source performs a raster scan and traverses across the substrate increasing the temperature of the substrate significantly as the scan progresses. Figure 7 shows the relation between the melt pool area and the melt pool depth for a complete scan of an IN100 sample. Since the dominant thermal gradient is along the vertical direction, an increase in the melt pool area is expected to increase the melt depth. The linear relation in Fig. 7 reveals that if the melt pool area is kept constant at a desired value, a uniform melt depth can possibly be achieved. The plot also shows the relation between the average melt pool temperature and the melt pool depth for the same sample. Again, the linear relation reveals that if the average melt pool temperature is kept constant at a desired value, a uniform melt depth can possibly be achieved.

The objective of the feedback control trials is aimed at determining the effect of maintaining a constant average melt pool temperature on the deposit characteristics. Data from a thermal imaging camera is used to compute the average melt pool temperature and an adaptive controller is programmed to adjust the laser power accordingly [15]. The scan speed and the number of repeat scans are not changed during the run. The adaptive control trials are able to appropriately control the laser power and thus the average melt pool temperature during SLE processing and produce uniform deposits. As shown in Figs. 8 (a) and 8 (b), both melt depth uniformity and deposit height uniformity is achieved due to control of the average melt pool temperature in Fig. 8(b) compared to a sample processed under open loop control in Fig. (a).

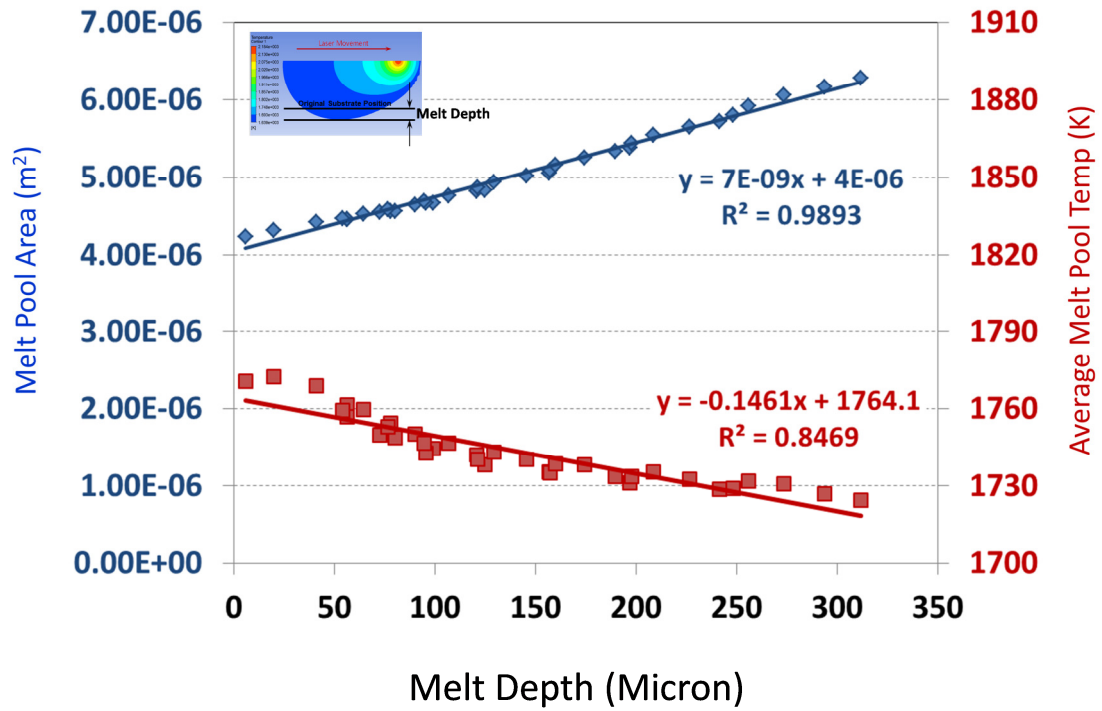


**Figure 7.** Variations of the melt pool area and average melt pool temperature with the melt depth for IN100.

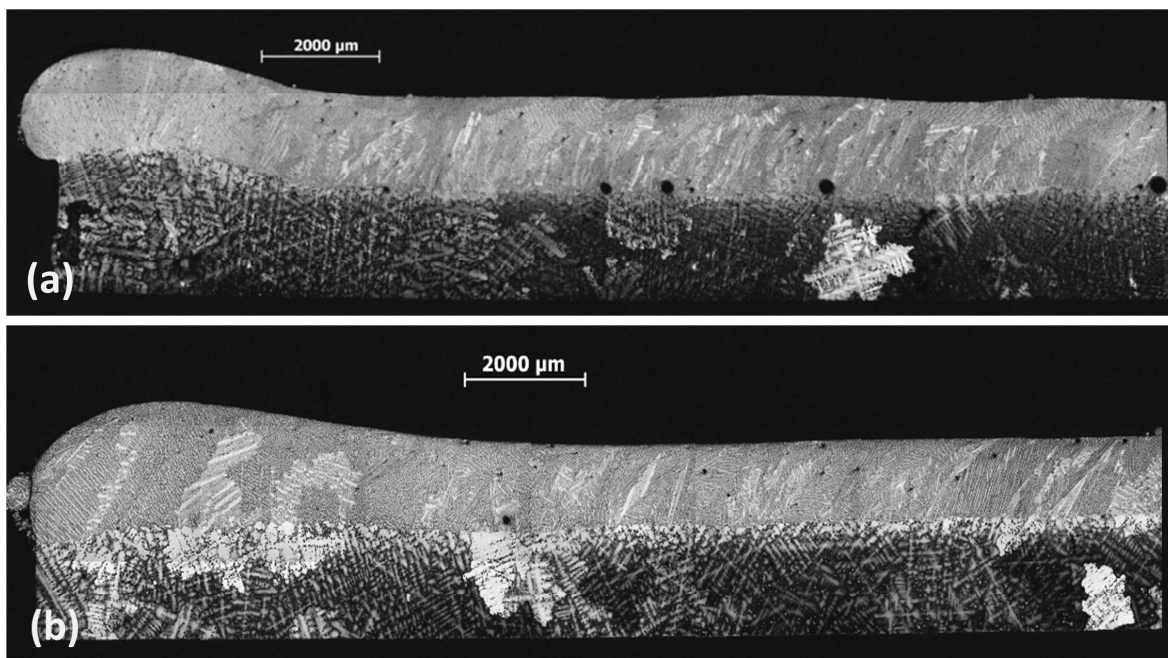


**Figure 8.** Transverse cross section of a representative (a) open-loop specimen and (b) closed-loop specimen for IN100.

## **Conclusions**

In the current work, a two dimensional CFD-based modeling scheme is implemented to simulate the SLE process using a single platform for different equiaxed superalloys. The simulation work is compared with the experimental melt pool depth profile and reasonably good agreement is achieved for IN100, René 80 and MAR-M247. Laser power, scan speed and number of repeat scans are varied for each experimental runs and their effects on the SLE deposit have been analyzed. Excellent agreement is obtained between simulation and experimental results for the melt depth for wide range of SLE processing parameters. Feedback control is implemented to accurately control the average melt pool temperature, showing excellent results in maintaining a uniform deposit as well as a uniform melt depth. A future objective is to develop a simulation map that will allow accurate prediction of the microstructure development as a function of operating parameters and melt pool conditions in superalloys processed through SLE.

## **Acknowledgments**

This work is sponsored by the Office of Naval Research through grants N00014-11-1-0670 and N00014-14-1-0658. The first author would like to thank Shashank Holenarasipura Raghu for his assistance with metallography.

## **References**

1. Anderson TD, DuPont JN, DebRoy T. Origin of Stray Grain Formation in Single-Crystal Superalloy Weld Pools from Heat Transfer and Fluid Flow Modeling. *Acta Materialia*. 2010; 58(4):1441-54.
2. Childs THC, Hauser C, Badrossamay M. Mapping and Modelling Single Scan Track Formation in Direct Metal Selective Laser Melting. *CIRP Annals – Manufacturing Technology*. 2004; 53(1):191-4.
3. Cline, H. and T. Anthony. Heat Treating and Melting Material with a Scanning Laser or Electron Beam. *Journal of Applied Physics*, 1977; 48(9):3895-3900.
4. Gaumann, M. Epitaxial Laser Metal Forming of a Single Crystal Superalloy. PhD Thesis (EPFL Lausanne), 1999.
5. Christensen, N., V.d.L. Davies, and K. Gjermundsen. Distribution of Temperatures in Arc Welding. *British Welding Journal*, 1965; 12(2):54-75.
6. Goldak, J., A. Chakravarti, and M. Bibby. A New Finite Element Model for Welding Heat Sources. *Metallurgical Transactions B*, 1984; 15(2):299-305.
7. Acharya, R., et al. CFD Modeling of Microstructural Development in the Scanning Laser Epitaxy Process. *CFD Modeling and Simulation in Materials Processing*, 2012; 197-204.
8. Chan, C.L., J. Mazumder, and M.M. Chen, Effect of Surface Tension Gradient Driven Convection in a Laser Melt Pool: Three-Dimensional Perturbation Model. *Journal of Applied Physics*, 1988; 64(11):6166.
9. Chande, T. and J. Mazumder, Mass Transport in Laser Surface Alloying: Iron-Nickel System. *Applied Physics Letters*, 1982; 41(1):42-43. C. T. Chang, ‘Low emissions combustors development and testing’, (Paper presented at National Aeronautics and Space Administration).

10. Acharya, R., et al. A Coupled Thermal, Fluid Flow, and Solidification Model for the Processing of Single-Crystal Alloy CMSX-4 Through Scanning Laser Epitaxy for Turbine Engine Hot-Section Component Repair (Part I). *Metallurgical and Materials Transactions B*, 2014; 45(6): 2247-2261.
11. Acharya, R., et al. Additive Manufacturing of IN100 Superalloy through Scanning Laser Epitaxy for Turbine Engine Hot-Section Component Repair: Process Development, Modeling, Microstructural Characterization, and Process Control. *Metallurgical and Materials Transactions A*, 2015 – *to appear*.
12. Quested, P., et al., Measurement and estimation of Thermophysical Properties of Nickel Based Superalloys. *Materials Science and Technology*, 2009; 25(2):154-162.
13. I. Hamill. Implementation of a Solidification Model in CFX-5. CFX Ltd.2003.
14. W. L. S. McCabe, Julian C., Harriot, Peter. *Unit Operations of Chemical Engineering*, 7 ed. New York: McGraw-Hill, 2005.
15. R. Bansal, Ph.D. Thesis, Georgia Inst. Technol., Atlanta 2013